

# On the Progenitor of the Crab Pulsar

Elvira Cruz-Cruz,<sup>1\*</sup> and C. S. Kochanek,<sup>1,2</sup>

<sup>1</sup>*Department of Astronomy, The Ohio State University, 140 West 18th Avenue, Columbus, OH 43210, USA*

<sup>2</sup>*Center for Cosmology and AstroParticle Physics (CCAPP), The Ohio State University, 191 W. Woodruff Avenue, Columbus, OH 43210, USA*

Accepted XXX. Received YYY; in original form ZZZ

## ABSTRACT

The Crab supernova is interesting because we know that it was not a binary at death, the outcome was a neutron star, and because of the supernova remnant’s apparently low energy and mass. Using Gaia EDR3 parallaxes and photometry, we examine the stellar population local to the Crab in a cylinder with a projected radius of 100 pc and parallax range  $0.427 < \varpi < 0.619$  mas set by the uncertainties in the Crab’s parallax. We also individually model the most luminous stars local to the Crab. The two most luminous stars are blue, roughly main sequence stars with masses of  $\sim 11M_{\odot}$ . We estimate the stellar population’s age distribution using Solar metallicity PARSEC isochrones. The estimated age distribution of the  $205 M_G < 0$  stars modestly favor lower mass stars consistent with an AGB star or a lower mass binary merger as the progenitor, but we cannot rule out higher masses. This may be driven by contamination due to the  $\sim 700$  pc length of the cylinder in distance.

**Key words:** supernovae – supernova remnant, progenitor

## 1 INTRODUCTION

We need to understand the progenitors of core-collapse supernovae (ccSNe) to understand the final stages of massive stellar evolution and their relation to supernovae and their remnants. Understanding the deaths of massive stars is crucial for comprehending their evolution, the role of binaries, and the origins of the systems that merge and produce gravitational waves. In particular we would like to know the masses of SN progenitors. Three methods have been used to constrain progenitor masses: (1) direct observations of progenitors, (2) X-ray estimates of supernovae remnant (SNR) compositions; and (3) analyses of the stellar populations local to the supernovae. The latter two methods are indirect but have the advantage that they can be used long after the explosion occurred.

The progenitors of Type II-P SNe are the best constrained thanks to direct observational detections of their progenitors in (mostly) archival HST data (e.g., Smartt et al. 2002a,b, 2009; Van Dyk et al. 2003, 2012; Li et al. 2006, 2007; Maund et al. 2005, 2011, 2014; Hendry et al. 2006; Smith et al. 2011; Fraser et al. 2014). Smartt et al. (2009), using 8 mass estimates and 12 upper limits for Type IIP SN progenitors found a minimum mass of  $M < 8.5^{+1.0}_{-1.5}M_{\odot}$  and a maximum mass of  $M_{max} = 16.5 \pm 1.5M_{\odot}$  assuming a Salpeter IMF. The progenitors to Type IIP supernovae are all red supergiants (RSG) (Smartt et al. 2009). In a later review of 18 mass estimates and 27 upper limits, Smartt (2015) found an upper mass limit for RSGs exploding as Type II SN of about  $18M_{\odot}$ .

Since stellar models predict that RSGs of up to  $30M_{\odot}$  undergo core-collapse and could produce Type II SN, the missing  $18-30M_{\odot}$  progenitors has been termed the red supergiant problem. Since then there has been ongoing debate about the existence of this mass range problem (e.g., Kochanek et al. 2012; Kochanek 2020; Beasor et al. 2020; Walmswell & Eldridge 2012; Groh et al. 2013; Davies & Beasor 2018, 2020; Strotjohann et al. 2024). There are fewer direct detections of progenitors to Type Ibc supernovae because stripped stars tend to be optically faint and difficult to detect (e.g., Eldridge et al. 2013; Folatelli et al. 2016; Johnson et al. 2017; Kilpatrick et al. 2021; Yoon et al. 2012).

A second method for understanding supernovae and their progenitors is to analyze the X-ray emission from the ejecta. Katsuda et al. (2018) made progenitor mass estimates for 33 core-collapse SNRs in our Galaxy and the Small and Large Magellanic Clouds, focusing on the Fe/Si abundance ratio. They argue that the Fe/Si ratio is the best estimate of the progenitor’s CO core mass and thus the initial progenitor mass  $M_{ZAMS}$ . Katsuda et al. (2018) splits the sample into three mass bins where  $M_{ZAMS} < 15M_{\odot}$ ,  $15M_{\odot} < M_{ZAMS} < 22.5M_{\odot}$ , and  $22.5M_{\odot} < M_{ZAMS}$  to model the bin fraction with and without a mass cutoff. They argue that the observed distribution better agrees with models lacking the mass cutoff implied by the red supergiant problem.

The third method is to analyze the stellar populations near both SNe and SNRs in external galaxies. The color-magnitude diagram (CMD) of the nearby stars is modeled with isochrones to derive the local star formation history, which then provides a probability distribution for the mass of the star which exploded. For example, Jennings et al. (2014) found supernovae remnant progenitor mass distributions for

\* E-mail: cruz-cruz.1@osu.edu (ECC)

M31 and M33, [Auchetti et al. \(2019\)](#) did so for the Small Magellanic Cloud, [Murphy et al. \(2011\)](#) did so for SN 2011dh, and [Williams et al. \(2014\)](#) ([Díaz-Rodríguez et al. 2021](#)) compiled progenitor mass constraints for 17 (22) historic core-collapse supernovae. [Díaz-Rodríguez et al. \(2021\)](#), for example, finds a progenitor mass distribution with a minimum mass of  $M_{min} = 8.60_{-0.41}^{+0.37} M_{\odot}$  and a slope of  $\alpha = -2.61_{-1.18}^{+1.05}$ .

Gaia ([Gaia Collaboration et al. 2016, 2021](#)) makes applying the stellar population analysis method feasible in our Galaxy ([Kochanek 2022](#)). Galactic SNRs have the advantage that we frequently know the result of the explosion and the binarity of the progenitor (e.g., [Ilovaisky & Lequeux 1972](#); [Boubert et al. 2017](#); [Kochanek 2018](#); [Fortin et al. 2024](#)). Accurate parallaxes allow both the selection of stars local to the SNR and the determination of their luminosities. Three dimensional dust maps (e.g., [Bovy et al. 2016](#); [Green et al. 2019](#)) enabled by Gaia help to constrain the individual stellar extinctions. [Kochanek \(2022\)](#) and [Murphy et al. \(2024\)](#) successfully applied this method to the Vela pulsar. [Kochanek \(2022\)](#) found a progenitor mass estimate of  $\leq 15 M_{\odot}$  and [Murphy et al. \(2024\)](#) found evidence that Vela’s progenitor was the product of a binary merger. Suitable candidates for this method do require a well-constrained SNR distance which is frequently a problem, although [Kochanek et al. \(2024\)](#) demonstrated a method which should provide accurate distances to any SNR with modest extinction. One good candidate is the Crab SNR where Gaia DR3 ([Gaia Collaboration et al. 2021](#)) and VLBI observations of the pulsar ([Lin et al. 2023](#)) provide well-measured distances, we know that the outcome of the explosion was a neutron star (e.g., [Staelin & Reifenstein 1968](#); [Comella et al. 1969](#)), and that the system was not a binary at death ([Kochanek 2018](#)).

The origin of the Crab SNe (i.e., ccSNe or electron capture SNe), and remnant, has long been a topic of discussion (e.g., [Clark & Stephenson 1977](#); [Davidson & Fesen 1985](#); [Collins et al. 1999](#)). The Crab nebula and pulsar are the remnants of SN 1054 (e.g., [Duyvendak 1942](#); [Mayall & Oort 1942](#); [Staelin & Reifenstein 1968](#); [Comella et al. 1969](#)). The SNR appears to be low mass and have a low kinetic energy of  $\approx 10^{49}$  erg, lower than the expected kinetic energy of a core-collapse supernova  $\approx 10^{51}$  erg, (e.g., [MacAlpine et al. 1989](#); [Bietenholz et al. 1991](#); [Fesen et al. 1997](#); [Smith 2003](#)). The SN was a very luminous event with a peak absolute visual magnitude of  $-18$  mag (e.g., [Chevalier 1977](#); [Trimble 1973](#); [Miller 1973](#)) that is brighter than typical Type II ccSNe (e.g., [Li et al. 2011](#)). [Smith \(2013\)](#) argues that the Crab was a Type II-P supernova caused by a sub-energetic electron-capture explosion of an  $8 - 10 M_{\odot}$  super-AGB star. Electron capture SNe are generally associated with the mass range of extreme AGB stars ([Miyaji et al. 1980](#); [Nomoto et al. 1982](#); [Nomoto 1987](#)), although the exact mass range depends on the model (e.g., [Poelarends et al. \(2008\)](#) and [Limongi et al. \(2024\)](#) find  $9.00 - 9.25 M_{\odot}$  and  $8.5 - 9.2 M_{\odot}$ , respectively). They are predicted to be underluminous and underenergetic (e.g., [Kitauro et al. 2006](#)). In the [Smith \(2013\)](#) scenario, the high luminosity is not driven by the normal emissions of the SN, but instead by shock heating the dense circumstellar medium of the AGB star progenitor. Thus, under this hypothesis we would expect to find a local stellar population with few or no massive stars ( $\gtrsim 10 M_{\odot}$ ).

More recently, [Omand et al. \(2024\)](#) explored an alternate theory for the origin of SN 1054’s peak luminosity. They fit a

pulsar-driven supernova model to the historical observations of SN 1054’s luminosity. Their model suggests an initial spin-down luminosity of the Crab pulsar of around  $10^{43-45}$  erg/s with a spin-down timescale of 1-100 days and a low supernova explosion energy of  $\sim 10^{49} - 10^{50}$  erg ([Omand et al. 2024](#)). This implies a high initial pulsar rotational energy of  $\sim 10^{50}$  erg and an initial spin period of  $\sim 13$  ms (other estimates of the initial spin periods are 15-20 ms, [Kou & Tong \(2015\)](#), and 3-5 ms, [Atoyan \(1999\)](#)). They propose that the supernova underwent a “blowout”, where the pulsar wind nebula broke through the ejecta shell, leaving dense filaments behind while accelerating the outer ejecta 50-200 years after the explosion.

Here we apply the [Kochanek \(2022\)](#) approach for Vela to the Crab. In Section 2 we describe the selection of stars surrounding the Crab pulsar and the spectral energy distributions (SED) of the most luminous stars. In Section 3 we analyze the age distribution of the stars to estimate the likely mass of the Crab’s progenitor. In Section 4 we discuss the results. In Section 5 we summarize our findings and potential future applications.

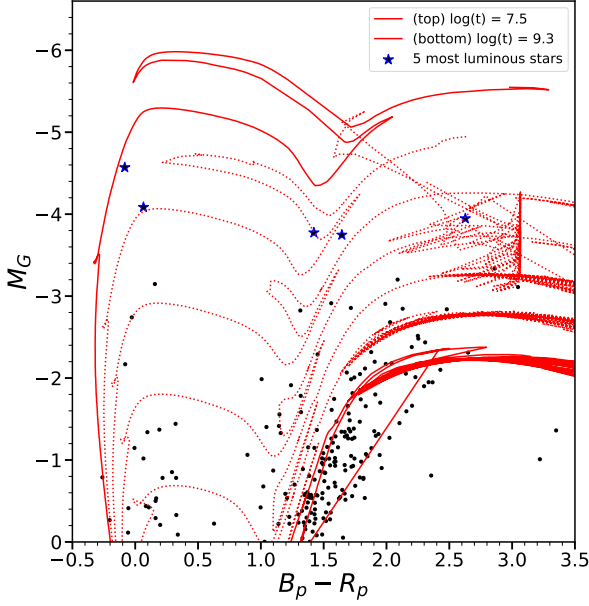
## 2 THE SURROUNDING STELLAR POPULATION

We select stars near the Crab Pulsar using Gaia DR3 ([Gaia Collaboration et al. 2016, 2021](#)). Each star is required to have a parallax and all three Gaia Magnitudes ( $G$ ,  $R_p$  and  $B_p$  bands). We use the position (J2000 05:34:31.947, +22:00:52.153) of the Crab pulsar from [Gaia Collaboration et al. \(2021\)](#) as the center. We use a weighted average parallax of  $\varpi = 0.523 \pm 0.048$  mas ( $d = 1.912_{-0.30}^{+0.43}$  kpc) for the Crab, combining the Gaia ( $\varpi = 0.511 \pm 0.078$  mas, [Gaia Collaboration et al. 2021](#)), and VLBI ( $\varpi = 0.523 \pm 0.048$  mas, [Lin et al. 2023](#)) parallaxes. We first search for stars in a region centered on the position of the Crab with a maximum search angular size,  $\theta = \sin^{-1}(R/D) = 3.58^\circ$ , where  $D = 2$  kpc and  $R = 125$  pc, with parallaxes  $0 < \varpi < 1$  mas. We use a magnitude limit of  $G < 12$  to include stars with absolute magnitudes  $M_G \leq 0$  mag and masses that are  $M \gtrsim 1 M_{\odot}$ .

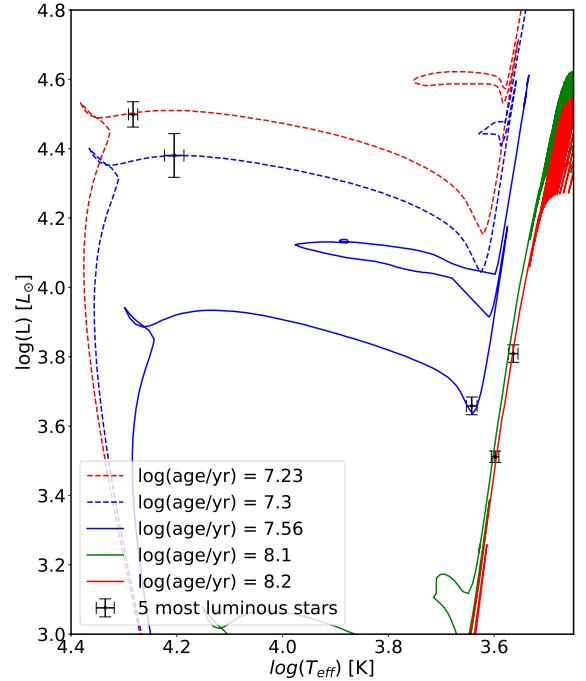
Geometrically the search region is a truncated cone and contains 1,525 stars. Next, we convert the search region from a truncated cone into a truncated cylinder, with a radius  $R = 100$  pc around the Crab. From the coordinates and parallax we form a vector ( $\vec{u}_*$ ) for the position of the star. The cross product ( $d_{\perp} = |\vec{u}_{cp} \times \vec{u}_*|$ ) with a unit vector pointing to the pulsar ( $\vec{u}_{cp}$ ) provides the separation perpendicular to the line of sight and we keep the 225 stars with  $d_{\perp} < R$  and parallaxes between  $0.427 < \varpi < 0.619$  mas, which is the  $2\sigma$  error range of the Crab’s weighted average parallax. The resulting length of the cylinder ( $\sim 700$  pc) is longer than desired, but it seemed better to be “inclusive” given the distance uncertainties. We used extinction estimates for each star from the 3-dimensional (3D) `combined19 mwdust` models ([Bovy et al. 2016](#)) which are based on [Green et al. \(2019\)](#) for the position of the Crab to obtain extinction corrected colors ( $B_p - R_p$ ) and absolute magnitudes ( $M_G$ ). We keep the 205 stars with  $-8 < M_G < 0$ ,  $-0.5 < B_p - R_p < 3.5$ . In practice, there are no  $M_G < -8$  mag stars in the sample. In Figure 1 we show the CMD of these stars with the 5 most luminous stars labeled with blue stars, and PARSEC (e.g., [Bressan et al. 2012](#); [Marigo et al. 2013](#); [Pastorelli et al. 2020](#)) isochrones spanning  $10^{7.5}$  to  $10^{9.3}$  years in steps of 0.3 dex.

**Table 1.** The luminous ( $M_G < -3.5$ ) stars near the Crab Pulsar.

Star	$\chi^2/N_{dof}$	$\log(T_*)[K]$	$\log(L_*)[L_\odot]$	$M_*[M_\odot]$	$\log(t)[yr]$	Sep [pc]	Comments
HD 36879	1.94	$4.205 \pm 0.018$	$4.381 \pm 0.063$	10.74 – 11.66	7.27 – 7.33	21.16	O7V C
HD 243780	3.86	$3.643 \pm 0.010$	$3.658 \pm 0.026$	6.38 – 8.26	7.54 – 7.81	55.84	B0 E
HD 36547	2.18	$4.283 \pm 0.009$	$4.499 \pm 0.037$	11.99 – 12.54	7.22 – 7.25	53.18	B1III C
IRAS 05310+2411	2.34	$3.598 \pm 0.007$	$3.512 \pm 0.017$	4.18 – 5.23	7.97 – 8.26	70.77	No spectral type
IRAS 05361+2406	4.53	$3.564 \pm 0.009$	$3.809 \pm 0.025$	2.21 – 4.92	8.08 – 9.05	93.38	Long Period Variable, No spectral type


**Figure 1.** Extinction corrected color-magnitude diagram of the stars local to the Crab from Gaia EDR3. Solar metallicity PARSEC isochrones are shown in red in age steps of 0.3 dex (top, solid:  $\log_{10}(t) = 7.5$ ; bottom, solid:  $\log_{10}(t) = 9.3$ ). The blue stars are the 5 most luminous stars for which we did individual SED fits.

We first focus on these 5 most luminous stars ( $M_G < -3.5$ ) and fit their spectral energy distributions (SEDs) to estimate luminosities, temperatures and extinctions. We limit the SED fits to the most luminous stars because we are interested in the most massive and youngest stars local to the Crab. We use DUSTY (Elitzur & Ivezić 2001) inside a Markov Chain Monte Carlo (MCMC) driver to optimize the SED fits and their uncertainties following methods of Adams et al. (2017) and Kochanek (2022). For the coolest stars we use MARCS (Gustafsson et al. 2008) stellar model atmospheres and Castelli & Kurucz (2003) otherwise. We used UV, optical, near-IR and mid-IR magnitudes from Thompson et al. (1978) or Wessellius et al. (1982), Johnson et al. (1966) and ATLAS-REFCAT (Tonry et al. 2018), 2MASS (Cutri et al. 2003) and ALLWISE (Cutri et al. 2021). We use temperature and extinction priors based on spectral types reported in VizieR (Ochsenbein et al. 2000) and the widths of the tem-


**Figure 2.** Estimated luminosities and temperatures of the 5 most luminous stars obtained from SED fits as compared to PARSEC Solar metallicity isochrones with ages from  $10^{6.3} yr$  (dashed red) to  $10^{10.1} yr$  (dashed grey) in steps of 0.01 dex.

perature and extinction prior errors were  $\pm 1000K$  and  $\pm 0.1$  mag.

Table 1 provides the estimated age, mass range, luminosity, temperature, known or unknown spectral classification, transverse distance from the Crab pulsar, and the goodness of the SED fits. The age and mass constraints were obtained by finding the PARSEC isochrone ages and masses where the luminosity and temperature are within the 1-sigma error range of the SED fits. We use Solar metallicity PARSEC isochrones with ages from  $10^{6.3} yr$  to  $10^{10.1} yr$  in steps of 0.01 dex. The five most luminous stars have luminosities of  $10^{4.38 \pm 0.06} L_\odot$ ,  $10^{3.65 \pm 0.03} L_\odot$ ,  $10^{4.49 \pm 0.04} L_\odot$ ,  $10^{3.51 \pm 0.02} L_\odot$ ,  $10^{3.81 \pm 0.03} L_\odot$ , with masses of  $11.19 M_\odot \pm 0.07 M_\odot$ ,  $7.32 M_\odot \pm 0.15 M_\odot$ ,  $12.33 M_\odot \pm 0.09 M_\odot$ ,  $4.75 M_\odot \pm 0.06 M_\odot$ ,  $4.34 M_\odot \pm 0.08 M_\odot$ ,

respectively. The two most massive stars both lie near the main sequence and have luminous/early spectral types (O7 and B1). The other 3 stars are much less massive red giants. The spectral type reported for HD243780 (B0 E) is inconsistent with its location on the CMD and the SED model. We show the SED models in Appendix A. Figure 2 shows the resulting SED fit temperatures and luminosities of the 5 most luminous stars on a Hertzsprung-Russell diagram.

### 3 PROGENITOR MASS ANALYSIS

The next step in estimating the progenitor mass of the Crab is to find the age distribution of the selected stars. We use 13 age bins ( $i = 1 \dots 13$ ) with 0.3 dex widths. We assume single star evolution and Solar metallicity. We randomly draw  $N_{\text{trial}} = 3 \times 10^8$  stars from a Salpeter IMF with a minimum mass of  $M_{\text{min}} = 1M_{\odot}$ . We obtain their color and magnitudes using the PARSEC isochrone models sampled with  $\Delta \log t = 0.01$  dex (Bressan et al. 2012; Marigo et al. 2013; Pastorelli et al. 2020). We create the density maps  $F_{jk}(t_i) = F_{jk}^i$  of the stars in a Gaia CMD where  $i, j$ , and  $k$  index the time, absolute magnitude, and color, respectively. Each modeled star is created by uniformly selecting a time between  $t_{\text{min},i}$  and  $t_{\text{max},i}$ , corresponding to a constant star formation rate for each age bin. A star is added to the density map if the chosen mass still exists on the isochrone and the star lies in the absolute magnitude range of  $0.0 > M_G > -8.0$  (index  $j$ ) and the color range  $-0.5 < B_p - R_p < 3.5$  (index  $k$ ). For each star falling within these ranges of color and absolute magnitude, we add a 1 to the cell  $[j, k]$  corresponding to their color and magnitude. We do not include either observed or model stars that are either too red, too blue, or too luminous. We test the effects of this selection by creating maps that have these stars added to the edges of the density distributions, but this had no effect on the results (see Section 4).

We apply the `mw dust` extinction corrections to the observed stars surrounding the Crab and compare the stars to the density maps using their extinction corrected photometry (Fig. 1). We assume that these `mw dust` estimates are correct on average. We examined the effects of extinction uncertainties on the model density maps by also producing density maps with random Gaussian extinctions of  $\sigma_{E(B-V)} = 0.01, 0.03$  and 0.1 mag added to each trial star.

For a constant star formation rate (SFR), the formation rate by mass for  $M > M_{\text{min}}$  is

$$\frac{dN}{dMdt} = \frac{(x-2)SFR}{M_{\text{min}}^2} \left( \frac{M}{M_{\text{min}}} \right)^{-x} \quad (1)$$

with  $x = 2.35$  and a mean mass of  $\langle M \rangle = (x-1)M_{\text{min}}/(x-2)$ . The age bins are in logarithmic time intervals,  $t_{\text{min},i} < t < t_{\text{max},i}$ , where  $\Delta t = t_{\text{max},i} - t_{\text{min},i}$ . Since the  $SFR_i$  is constant, the number of  $M > M_{\text{min}}$  stars formed in each interval is  $N_i = SFR_i \Delta t_i / \langle M \rangle$ . The number of stars that die in a short time interval  $\delta t$  today is

$$N_i \frac{\delta t}{\Delta t_i} \left[ \left( \frac{M(t_{\text{min},i})}{M_{\text{min}}} \right)^{(1-x)} - \left( \frac{M(t_{\text{max},i})}{M_{\text{min}}} \right)^{(1-x)} \right] = N_i S_i \delta t \quad (2)$$

where  $M(t)$  is the most massive surviving star on the isochrone, and  $S_i \delta t$  is the fraction of  $M > M_{\text{min}}$  stars that

died in the last  $\delta t$  years. A full derivation of Equation 2 is in Appendix B.

The observed stars can be placed on the absolute magnitude and color grid in the same manner, with  $N_{jk}^*$  stars in a pixel and  $\sum_{jk} N_{jk}^* = N^* = 205$ . The number of model stars in a given magnitude and color bin is  $N_{jk} = \sum_i \alpha_i F_{jk}^i$ , where  $\alpha_i$  is proportional to the star formation rate of age bin  $i$ , and the model has a total of  $N = \sum_{jk} N_{jk}$  stars. The Poisson probability of finding the observed number of stars in a bin of color and magnitude is

$$\frac{N_{jk}^{N_{jk}^*} e^{-N_{jk}}}{N_{jk}^{N_{jk}^*}!}, \quad (3)$$

so the logarithm of the likelihood for all  $N^*$  stars is

$$\ln L = \sum_{jk} \ln \left( r N_{jk}^{N_{jk}^*} \right) - \sum_{jk} r N_{jk}, \quad (4)$$

where the first term is the sum over bins containing stars and the second is the sum over all bins. We discard the factorial  $N_{jk}^{N_{jk}^*}!$  because the calculation depends only on likelihood differences and not the absolute likelihood. Empty cells of  $N_{jk}$  are filled with a small number ( $1 \times 10^{-32}$ ) to avoid numerical problems.

We introduced a "re-normalization" factor  $r$  in Equation 5. Equation 5 with  $r = 1$  will include Poisson fluctuations in  $N$  relative to  $N^*$ . However, we really want the probability for how the  $N^*$  stars are divided over the 13 age bins. If we choose

$$r = N_* \left[ \sum_{jk} \sum_i \alpha_i F_{jk}^i \right]^{-1}, \quad (5)$$

and then re-normalize  $\alpha_i \rightarrow r \alpha_i$  so that  $\sum_{jk} \sum_i \alpha_i F_{jk}^i \equiv N_*$ , the likelihood becomes the multinomial likelihood for how to divide the  $N_*$  stars over the age bins. Some age bins are susceptible to  $\log(N_i) \rightarrow -\infty$ . To prevent such numerical divergences, we add a weak prior of

$$-\lambda^{-2} \sum_i \left[ \ln \left( \frac{\alpha_i \Delta t_{i+1}}{\alpha_{i+1} \Delta t_i} \right) \right]^2 - \lambda^{-1} \sum_i \left[ \ln \left( \frac{\alpha_i}{\alpha_0} \right) \right]^2, \quad (6)$$

where  $\lambda = 6.91$ , which adds a penalty of unity to the likelihood if adjacent bins have star formation rates ( $SFR_i \approx N_i / \Delta t_i$ ) that differ by a factor of 1000, and the  $2^{nd}$  term with  $\alpha_0 = N_*/N$  penalizes not distributing the observed stars uniformly over the age bins.

We calculate the number of deaths in a time range  $\delta t$  with  $N_i S_i \delta t$ , where  $S_i$  is independent of  $\delta t$ . We want to find the probability that the progenitor was born from age bin  $i$  versus  $j$ , and therefore use the normalized probability for each age bin of

$$\frac{P_i}{P_{\text{tot}}} = \frac{N_i S_i}{\sum_{\text{all}} N_i S_i}, \quad (7)$$

is independent of  $\delta t$ , which has a total probability of unity.

We optimize the likelihood and estimate the uncertainties using the Monte Carlo Markov Chain (MCMC) driver in the `emcee` python package (Foreman-Mackey et al. 2013), with  $\log \alpha_i$  as the fit parameters. We uses 300 walkers each with



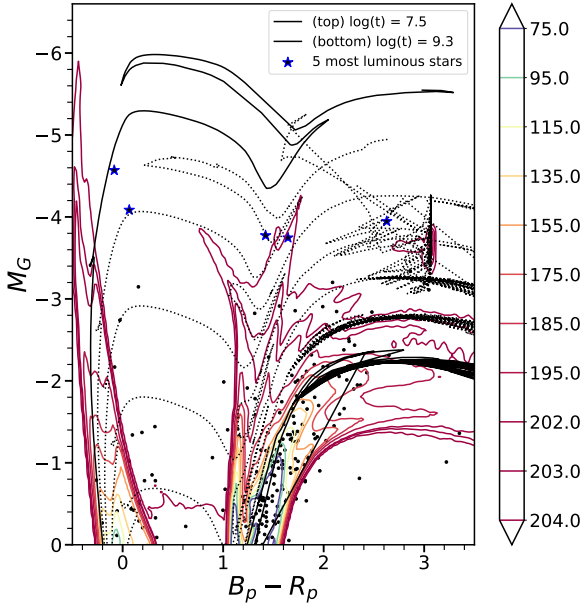


**Figure 3.** The black dots are the extinction corrected Gaia CMD of the stars near the Crab, and the curves are the Solar metallicity PARSEC isochrones with ages from  $10^{7.5}$ yr (top black) to  $10^{9.3}$ yr (bottom black) in steps of 0.3 dex. The model density contours are drawn at the level which encompasses the number of stars shown on the scale bar. The blue stars are the 5 most luminous stars near the Crab.

a chain length 10,000. We discard the first 1000 entries of each walker chain for determining uncertainties. Within the MCMC driver, these  $\log \alpha_i$  are re-normalized (Eq. 5) before calculating the likelihood.

#### 4 RESULTS

Figure 3 shows the resulting density contours for the distribution of the model stars in the CMD in the maximum likelihood model. The purple (magenta) contour lines show the low (high) stellar densities. The maximum densities lie along the main sequence and the red giant branch as expected and largely encompasses the observed stars.

Figures 4 and 5 show two different ways of viewing the distribution of stars in age. Figure 4 shows the distribution of the  $N_* = 205$  modeled stars over the age bins. The total number of stars exactly equals to 205 because of the renormalization in Equation 5. The fourth youngest age bin is  $10^{7.2}$ yr –  $10^{7.5}$ yr, which corresponds to mass ranges of  $9.1M_\odot - 13.1M_\odot$ , contains 2 stars and the following age bin  $10^{7.5}$ yr –  $10^{7.8}$ yr ( $6.5M_\odot - 9.1M_\odot$ ) contains 4 stars. Consistent with Figure 3, there are very few high mass stars in the region local to the Crab. The next two age bins corresponding to ages  $10^{7.8}$ yr –  $10^{8.4}$ yr ( $3.7M_\odot - 6.5M_\odot$ ) have a cumulative of 13 stars. The eighth oldest age bin ( $10^{8.4}$ yr –  $10^{8.7}$ yr) has 29 stars, which corresponds to  $2.9M_\odot - 3.7M_\odot$  stars. Figure 4 also shows the estimated ages of the 5 most luminous stars from the SED fits. The two youngest of these

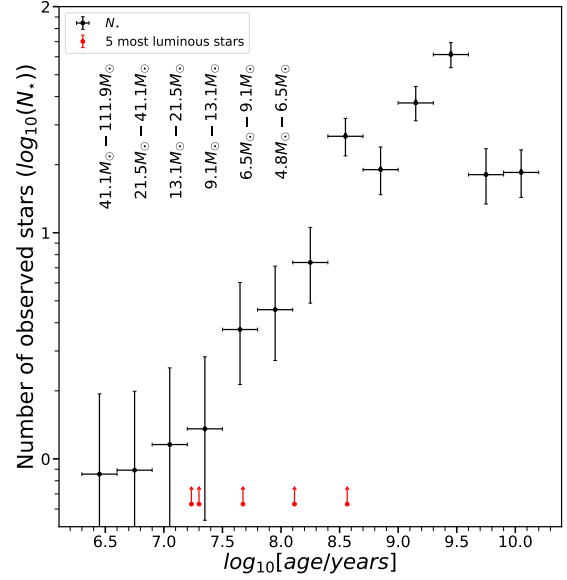


**Figure 4.** The number of observed stars assigned to each age bin (black points), where the horizontal bar shows the width of the bin in age. The mass range for each age bin is listed at the top left of the plot. The points and vertical errorbars are the median and 16 and 84 percentile ranges of the number of stars associated with each age bin. The red arrows show the estimated ages of the 5 individually modeled stars.

stars fall in the fourth youngest age bin ( $10^{7.2}$ yr –  $10^{7.5}$ yr or  $9.1M_\odot - 13.1M_\odot$ ), which is also consistent with the 4 stars found in the model. Figure 5 shows the number  $N_i$  of  $M > 1M_\odot$  stars formed per  $10^9$  years as a function of age. This is simply the observed number of stars (Fig. 4) divided by the fraction of the Monte Carlo trials leading to a star on the density grid and the temporal width of the bin.

Figure 6 compares the result in Fig. 4 to the result when we include a scatter in the extinction of  $\sigma_{ext} = 0.1, 0.03, 0.01$  mag, and Fig. 7 does the same but also includes stars which are too red or too blue on the grid edges. The qualitative structure of Fig. 4 is little changed by these variations.

Figures 8 and 9 show the differential and integral distributions in age of the number of stars expected to have died in the last  $\delta t = 10^5$ yr. The probabilities are low because if we took a random volume with this stellar age distribution, the probability of finding an SNR would be very low. By selecting the volume to contain an SNR, it is no longer random. This selection effect only affects the absolute probabilities and not the relative probabilities. Formally, we find that lower mass progenitors are favored, but the probability contrast between the lower and higher masses does not allow a very strong limit. If we focus on the differential probability, the age bins corresponding to stars which might be electron capture supernovae either directly or as a binary merger product (the  $10^{7.2}$ yr –  $10^{7.8}$ yr age bins with a mass range of  $6.5M_\odot - 13.1M_\odot$ ), they have median likelihoods roughly 5 times those of the higher mass ( $\geq 13.1M_\odot$ ) bins. However, if we consider the integral probability distri-

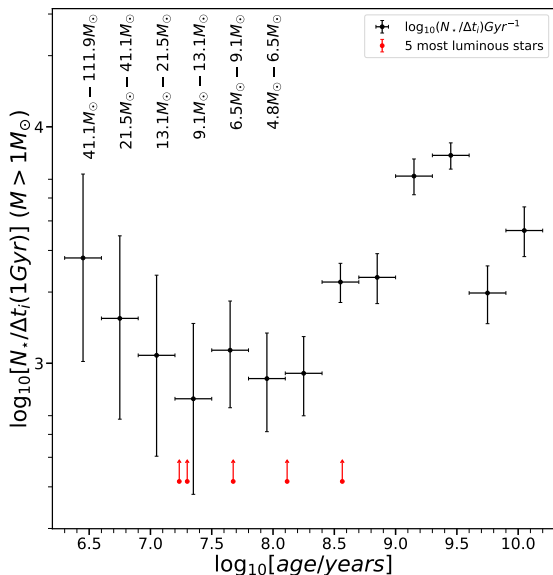


**Figure 5.** The number  $N_{*,i}$  of  $M > 1M_{\odot}$  stars formed in each age bin per  $10^9$  years. This corresponds to the number of observed stars shown in Figure 4 divided by the fraction of the Monte Carlo trials leading to a star on the density grid and the temporal age bin width,  $\Delta t_i$  (in units of  $1Gyr = 10^9yr$ ). The horizontal errors are the 0.3 dex widths of the age bins. The red arrows are the estimated ages of the 5 most luminous stars.

bution over this same age range, these two bins encompass only 64% of the probability. If we include the next lower age bin ( $10^{7.8}yr - 10^{8.1}yr$  with masses  $4.8M_{\odot} - 6.5M_{\odot}$ ), this increases to 76% of the probability. Essentially, the dynamic range of the differential probability distribution simply is not large enough to strongly rule out higher mass progenitors. The absence of any luminous stars for age bins younger than  $10^{7.2}$  years does suggest that these younger ages should be disfavored.

## 5 DISCUSSION

We examine the properties of the 205 stars with  $M_G < 0$  mag in a volume surrounding the Crab SNR. If we examine the five most luminous stars, we find that the two most luminous, HD 36879 and HD 36547, have luminosities, masses and ages of roughly  $10^{4.38 \pm 0.06} L_{\odot}$  ( $10^{4.49 \pm 0.04} L_{\odot}$ ),  $11.19M_{\odot} \pm 0.07M_{\odot}$  ( $12.33M_{\odot} \pm 0.09M_{\odot}$ ), and  $10^{7.30}yr$  ( $10^{7.23}yr$ ). Both are main sequence or perhaps slightly evolved blue stars. If we analyze the overall age distribution of all these stars and estimate the likely age distribution of stars which will have recently died, we find modest evidence in favor of lower mass stars, consistent with the proposal that the progenitor was an extreme AGB star leading to an electron capture supernova. The age bin where the progenitor could be the explosion of a binary merger (Zapartas et al. 2017) is roughly likely as the age bin corresponding to a directly formed AGB star. This is interesting since the Crab was not a binary at death

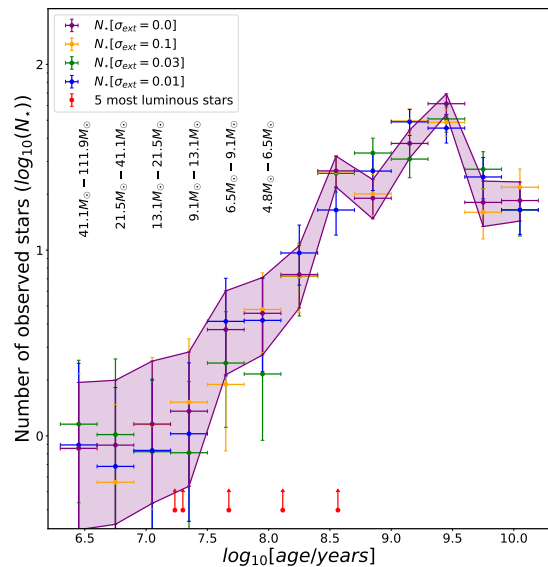


**Figure 6.** The model distributions of the observed stars in the age bins using density grids with an extinction scatter of  $\sigma_{ext} = 0.1, 0.03, 0.01$  (orange, green, and blue, respectively). The number of observed stars in Fig. 4 are plotted in purple,  $\sigma_{ext} = 0.0$ . The red arrows show the estimated ages of the 5 most luminous stars.

(Kochanek 2018), but almost all massive stars start in binary or high order systems (e.g., Moe & Di Stefano 2013; Sana et al. 2012). Unfortunately, the probability distribution does not drop sufficiently rapidly towards younger, higher mass progenitors to make a strong statistical case for this scenario. These results are stable with respect to the treatment of edge effects and allowing for noise in the stellar extinction estimates. One problem is that the parallax of the Crab is still sufficiently uncertain that we have had to use a distance range of roughly  $\sim 700$  pc which is much larger than desirable. Kochanek (2022), in a similar analysis of the stellar populations around Vela, found that contamination was already likely significant for a distance range of only  $\sim 200$  pc.

Nonetheless, this still seems to be an interesting new probe of Galactic SNRs given that we have so few. Kochanek et al. (2024) demonstrate a new method for estimating distances using multi-object Hectochelle spectrographs to search for the appearance of high velocity absorption features in stars behind the SNR that can provide distances to the typical SNR where there is no parallax for a remnant. Even in cases like the Crab with a parallax measurement, this approach may still do better than a direct parallax because it can average over the parallaxes of multiple stars rather than a single object. Some SNRs of particular interest are the ones which are presently interacting binaries (SS 433, HESS J0632+057, 1FGL J1018.6-5856; Blundell & Bowler 2004; Hinton et al. 2009; Corbet et al. 2011; Fermi LAT Collaboration et al. 2012, respectively) and the one relatively clear case of a binary unbound in the supernova (S147, Dingel et al. 2015; Kochanek 2021).

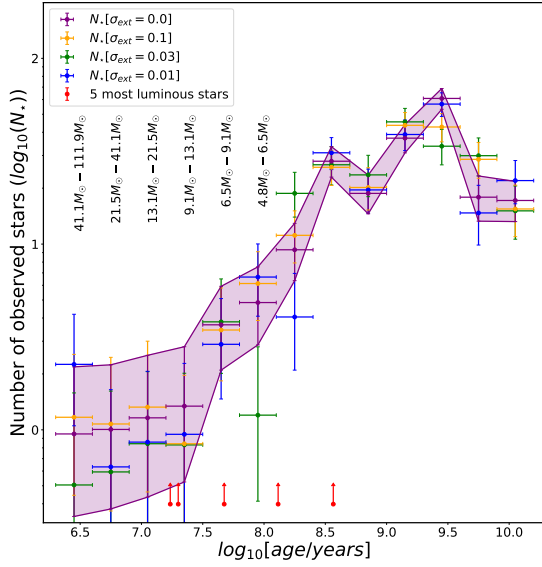


**Figure 7.** The model distribution of the observed stars across the age bins using modeled density maps with the alternate treatment of edge effects and  $\sigma_{ext} = 0.1, 0.03, 0.01$ , shown in orange, green, and blue, respectively. The vertical error bars span the 16<sup>th</sup> and 84<sup>th</sup> percentiles. The number of observed stars with the standard treatment of edge effects and no extinction scatter ( $\sigma_{ext} = 0.0$ ) are plotted in purple. The red arrows are the estimated ages of the 5 most luminous stars.

## DATA AVAILABILITY STATEMENT

All data used in this analysis are publicly available.

## ACKNOWLEDGEMENTS

Elvira Cruz-Cruz is supported by NASA FINESST Fellowship 80NSSC23K1444. Christopher S. Kochanek is supported by NSF grants AST-2307385 and AST-2407206. This research has made use of the VizieR catalogue access tool, CDS, Strasbourg, France (Ochsenbein 1996).

## REFERENCES

- Adams S. M., Kochanek C. S., Gerke J. R., Stanek K. Z., Dai X., 2017, *MNRAS*, **468**, 4968  
 Atoyan A. M., 1999, *A&A*, **346**, L49  
 Auchettl K., Lopez L. A., Badenes C., Ramirez-Ruiz E., Beacom J. F., Holland-Ashford T., 2019, *ApJ*, **871**, 64  
 Beasar E. R., Davies B., Smith N., van Loon J. T., Gehrz R. D., Figer D. F., 2020, *MNRAS*, **492**, 5994  
 Bietenholz M. F., Kronberg P. P., Hogg D. E., Wilson A. S., 1991, *ApJ*, **373**, L59  
 Blundell K. M., Bowler M. G., 2004, *ApJ*, **616**, L159  
 Boubert D., Fraser M., Evans N. W., Green D. A., Izzard R. G., 2017, *A&A*, **606**, A14  
 Bovy J., Rix H.-W., Green G. M., Schlafly E. F., Finkbeiner D. P., 2016, *ApJ*, **818**, 130

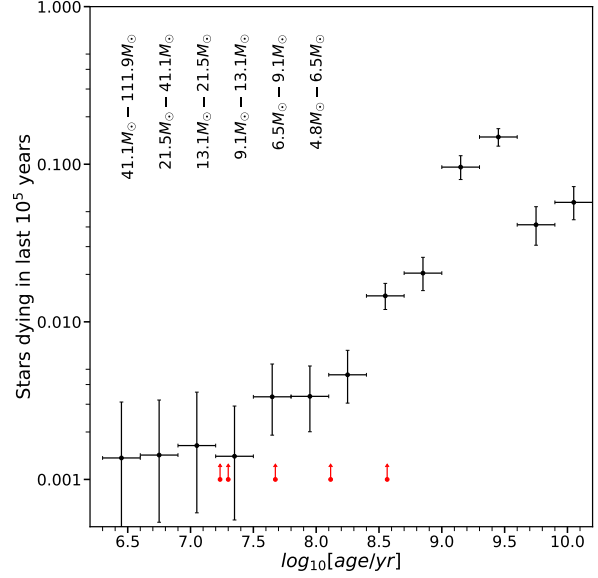


**Figure 8.** The number of stellar deaths over the last  $10^5$  years. The points are the estimate probability for each bin and its  $1\sigma$  confidence range. The horizontal error bars span the 0.3 dex age bin widths. The arrows show the ages of the 5 most luminous stars.

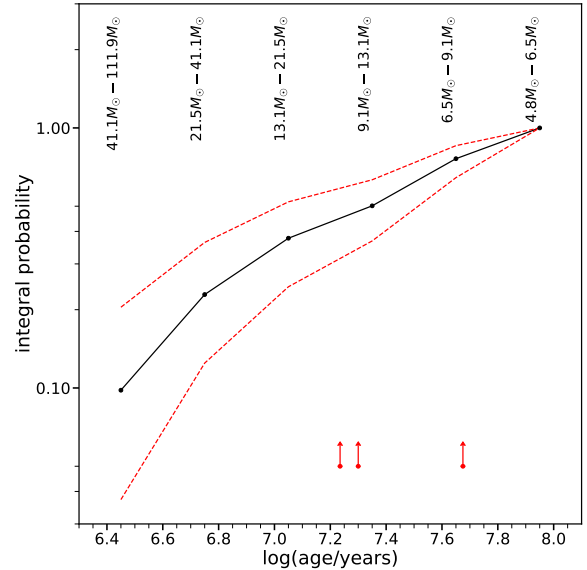


**Figure 9.** Integral probability distribution of the number of stellar deaths as a function of age. The red dashed lines are the  $1\sigma$  confidence range for the median number of stellar deaths within each age bin. The arrows are the age estimates of the 3 most luminous stars. The distribution is truncated at the oldest age bin that can produce a ccSN, albeit through the explosion of a merger remnant.

- Bressan A., Marigo P., Girardi L., Salasnich B., Dal Cero C., Rubele S., Nanni A., 2012, *MNRAS*, **427**, 127
- Castelli F., Kurucz R. L., 2003, in Piskunov N., Weiss W. W., Gray D. F., eds, Vol. 210, *Modelling of Stellar Atmospheres*. p. A20 ([arXiv:astro-ph/0405087](https://arxiv.org/abs/astro-ph/0405087)), [doi:10.48550/arXiv.astro-ph/0405087](https://doi.org/10.48550/arXiv.astro-ph/0405087)
- Chevalier R. A., 1977, in Schramm D. N., ed., *Astrophysics and Space Science Library* Vol. 66, *Supernovae*. p. 53, [doi:10.1007/978-94-010-1229-4\\_5](https://doi.org/10.1007/978-94-010-1229-4_5)
- Clark D. H., Stephenson F. R., 1977, *The historical supernovae*
- Collins George W. I., Claspy W. P., Martin J. C., 1999, *PASP*, **111**, 871
- Comella J. M., Craft H. D., Lovelace R. V. E., Sutton J. M., 1969, *Nature*, **221**, 453
- Corbet R. H. D., et al., 2011, *The Astronomer's Telegram*, **3221**, 1
- Cutri R. M., et al., 2003, *2MASS All Sky Catalog of point sources*.  
Cutri R. M., et al., 2021,
- Davidson K., Fesen R. A., 1985, *ARA&A*, **23**, 119
- Davies B., Beasor E. R., 2018, *MNRAS*, **474**, 2116
- Davies B., Beasor E. R., 2020, *MNRAS*, **496**, L142
- Díaz-Rodríguez M., Murphy J. W., Williams B. F., Dalcanton J. J., Dolphin A. E., 2021, *MNRAS*, **506**, 781
- Diñçel B., Neuhäuser R., Yerli S. K., Ankaý A., Tetzlaff N., Torres G., Mugrauer M., 2015, *MNRAS*, **448**, 3196
- Duyvendak J. J. L., 1942, *PASP*, **54**, 91
- Eldridge J. J., Fraser M., Smartt S. J., Maund J. R., Crockett R. M., 2013, *MNRAS*, **436**, 774
- Elitzur M., Ivezić Ž., 2001, *MNRAS*, **327**, 403
- Fermi LAT Collaboration et al., 2012, *Science*, **335**, 189
- Fesen R. A., Shull J. M., Hurford A. P., 1997, *AJ*, **113**, 354
- Folatelli G., et al., 2016, *ApJ*, **825**, L22
- Foreman-Mackey D., Hogg D. W., Lang D., Goodman J., 2013, *PASP*, **125**, 306
- Fortin F., Kalsi A., García F., Simaz-Bunzel A., Chaty S., 2024, *A&A*, **684**, A124
- Fraser M., et al., 2014, *MNRAS*, **439**, L56
- Gaia Collaboration et al., 2016, *A&A*, **595**, A1
- Gaia Collaboration et al., 2021, *A&A*, **649**, A1
- Green G. M., Schlafly E., Zucker C., Speagle J. S., Finkbeiner D., 2019, *ApJ*, **887**, 93
- Groh J. H., Meynet G., Georgy C., Ekström S., 2013, *A&A*, **558**, A131
- Gustafsson B., Edvardsson B., Eriksson K., Jørgensen U. G., Nordlund Å., Plez B., 2008, *A&A*, **486**, 951
- Hendry M. A., et al., 2006, *MNRAS*, **369**, 1303
- Hinton J. A., et al., 2009, *ApJ*, **690**, L101
- Ilovaisky S. A., Lequeux J., 1972, *A&A*, **18**, 169
- Jennings Z. G., Williams B. F., Murphy J. W., Dalcanton J. J., Gilbert K. M., Dolphin A. E., Weisz D. R., Fouesneau M., 2014, *ApJ*, **795**, 170
- Johnson H. L., Mitchell R. I., Iriarte B., Wisniewski W. Z., 1966, *Communications of the Lunar and Planetary Laboratory*, **4**, 99
- Johnson S. A., Kochanek C. S., Adams S. M., 2017, *MNRAS*, **472**, 3115
- Katsuda S., Takiwaki T., Tominaga N., Moriya T. J., Nakamura K., 2018, *ApJ*, **863**, 127
- Kilpatrick C. D., et al., 2021, *MNRAS*, **504**, 2073
- Kitaura F. S., Janka H. T., Hillebrandt W., 2006, *A&A*, **450**, 345
- Kochanek C. S., 2018, *MNRAS*, **473**, 1633
- Kochanek C. S., 2020, *MNRAS*, **493**, 4945
- Kochanek C. S., 2021, *MNRAS*, **507**, 5832
- Kochanek C. S., 2022, *MNRAS*, **511**, 3428
- Kochanek C. S., Khan R., Dai X., 2012, *ApJ*, **759**, 20
- Kochanek C. S., Raymond J. C., Caldwell N., 2024, *arXiv e-prints*, [p. arXiv:2403.13892](https://arxiv.org/abs/2403.13892)
- Kou F. F., Tong H., 2015, *MNRAS*, **450**, 1990
- Li W., Van Dyk S. D., Filippenko A. V., Cuillandre J.-C., Jha S., Bloom J. S., Riess A. G., Livio M., 2006, *ApJ*, **641**, 1060
- Li W., Wang X., Van Dyk S. D., Cuillandre J.-C., Foley R. J., Filippenko A. V., 2007, *ApJ*, **661**, 1013
- Li W., et al., 2011, *MNRAS*, **412**, 1441
- Limongi M., Roberti L., Chieffi A., Nomoto K., 2024, *ApJS*, **270**, 29
- Lin R., van Kerkwijk M. H., Kirsten F., Pen U.-L., Deller A. T., 2023, *ApJ*, **952**, 161
- MacAlpine G. M., McLaugh S. S., Mazzarella J. M., Uomoto A., 1989, *ApJ*, **342**, 364
- Marigo P., Bressan A., Nanni A., Girardi L., Pumo M. L., 2013, *MNRAS*, **434**, 488
- Maund J. R., Smartt S. J., Danziger I. J., 2005, *MNRAS*, **364**, L33
- Maund J. R., et al., 2011, *ApJ*, **739**, L37
- Maund J. R., Mattila S., Ramirez-Ruiz E., Eldridge J. J., 2014, *MNRAS*, **438**, 1577
- Mayall N. U., Oort J. H., 1942, *PASP*, **54**, 95
- Miller J. S., 1973, *ApJ*, **180**, L83
- Miyaji S., Nomoto K., Yokoi K., Sugimoto D., 1980, *PASJ*, **32**, 303
- Moe M., Di Stefano R., 2013, *ApJ*, **778**, 95
- Murphy J. W., Jennings Z. G., Williams B., Dalcanton J. J., Dolphin A. E., 2011, *ApJ*, **742**, L4
- Murphy J. W., Barrientos A. F., Andrae R., Guzman J., Williams B. F., Dalcanton J. J., Koplitz B., 2024, *arXiv e-prints*, [p. arXiv:2406.04075](https://arxiv.org/abs/2406.04075)
- Nomoto K., 1987, *ApJ*, **322**, 206
- Nomoto K., Sparks W. M., Fesen R. A., Gull T. R., Miyaji S., Sugimoto D., 1982, *Nature*, **299**, 803
- Ochsenbein F., 1996, *The VizieR database of astronomical catalogues*, [doi:10.26093/CDS/VIZIER](https://doi.org/10.26093/CDS/VIZIER), <https://vizier.cds.unistra.fr>
- Ochsenbein F., Bauer P., Marcout J., 2000, *A&AS*, **143**, 23
- Omand C. M. B., Sarin N., Temim T., 2024, *arXiv e-prints*, [p. arXiv:2404.19017](https://arxiv.org/abs/2404.19017)
- Pastorelli G., et al., 2020, *MNRAS*, **498**, 3283
- Poelarends A. J. T., Herwig F., Langer N., Heger A., 2008, *ApJ*, **675**, 614
- Sana H., et al., 2012, *Science*, **337**, 444
- Smartt S. J., 2015, *Publ. Astron. Soc. Australia*, **32**, e016
- Smartt S. J., Gilmore G. F., Tout C. A., Hodgkin S. T., 2002a, *ApJ*, **565**, 1089
- Smartt S. J., Vreeswijk P. M., Ramirez-Ruiz E., Gilmore G. F., Meikle W. P. S., Ferguson A. M. N., Knapen J. H., 2002b, *ApJ*, **572**, L147
- Smartt S. J., Eldridge J. J., Crockett R. M., Maund J. R., 2009, *MNRAS*, **395**, 1409
- Smith N., 2003, *MNRAS*, **346**, 885
- Smith N., 2013, *MNRAS*, **434**, 102
- Smith N., et al., 2011, *ApJ*, **732**, 63
- Staelin D. H., Reifstein Edward C. I., 1968, *Science*, **162**, 1481
- Strotjohann N. L., Ofek E. O., Gal-Yam A., 2024, *ApJ*, **964**, L27
- Thompson G. I., Nandy K., Jamar C., Monfils A., Houziaux L., Carnochan D. J., Wilson R., 1978, *Catalogue of stellar ultraviolet fluxes : a compilation of absolute stellar fluxes measured by the Sky Survey Telescope (S2/68) aboard the ESRO satellite TD-1 /*
- Tonry J. L., et al., 2018, *ApJ*, **867**, 105
- Trimble V., 1973, *PASP*, **85**, 579
- Van Dyk S. D., Li W., Filippenko A. V., 2003, *PASP*, **115**, 1289
- Van Dyk S. D., et al., 2012, *ApJ*, **756**, 131
- Walmswell J. J., Eldridge J. J., 2012, *MNRAS*, **419**, 2054
- Wesseliuss P. R., van Duinen R. J., de Jonge A. R. W., Aalders J. W. G., Luinge W., Wildeman K. J., 1982, *A&AS*, **49**, 427
- Williams B. F., Peterson S., Murphy J., Gilbert K., Dalcanton J. J., Dolphin A. E., Jennings Z. G., 2014, *ApJ*, **791**, 105
- Yoon S. C., Gräfener G., Vink J. S., Kozyreva A., Izzard R. G., 2012, *A&A*, **544**, L11
- Zapartas E., et al., 2017, *A&A*, **601**, A29



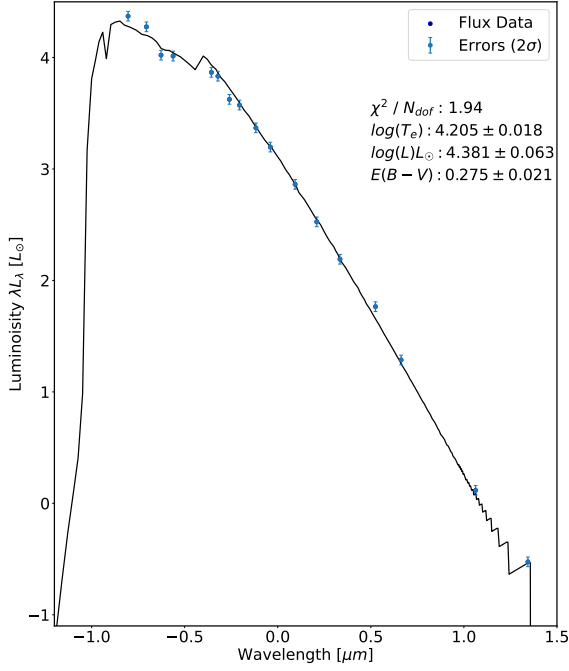


**Figure A1.** The SED of the O7V(n)(f)z C star HD 36879.

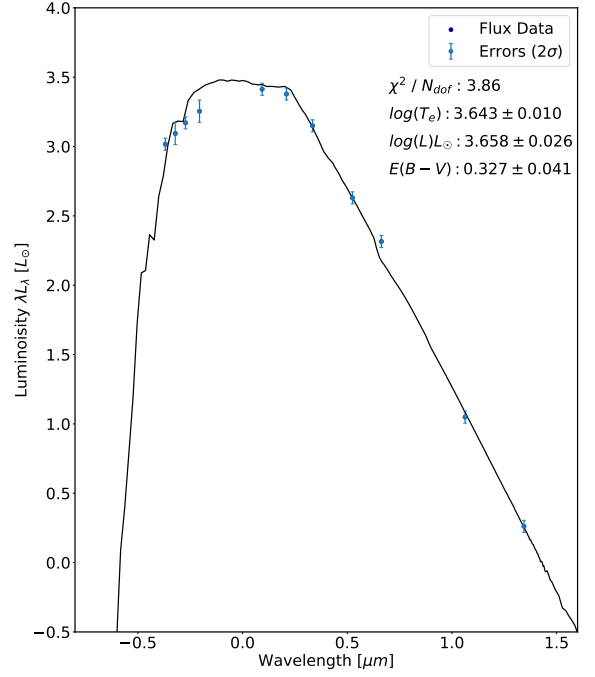


**Figure A2.** The SED of the B0 E Star HD 243780.

## APPENDIX A: SED FIT RESULTS

Figures A1 through A5 show the SED fits for each of the 5 most luminous stars found near the Crab.

## APPENDIX B: DERIVATION OF EQUATION 2

We start with Equation 1, for a constant star formation rate of stars with masses  $M > M_{min}$ , and a mean mass of  $\langle M \rangle = (x-1)M_{min}/(x-2)$ . If we integrate over  $M$ , we get the number of stars

$$N = \int_{t_{min}}^{t_{max}} \int_{M_{min}}^{\infty} dM \frac{dn}{dM dt} = \frac{SFR}{\langle M \rangle} \Delta t.$$

For an interval of ages where  $\Delta t = t_{max} - t_{min}$ , the number of stars dying within a time period  $\delta t$  is

$$\int_{t_{min}}^{t_{max}} dt \int_{M(t)}^{M(t+\delta t)} dM \frac{dn}{dM dt},$$

where  $M(t)$  is the mass of a star dying at time  $t$ . If we do the mass integral, we get

$$\int_{t_{min}}^{t_{max}} dt \frac{SFR}{\langle M \rangle} \left[ \left( \frac{M(t)}{M_{min}} \right)^{1-x} - \left( \frac{M(t+\delta t)}{M_{min}} \right)^{1-x} \right].$$

and then Taylor expand  $M(t+\delta t) = M(t) + (dM/dt)\delta t$  to

get

$$\int_{t_{min}}^{t_{max}} dt \frac{SFR}{\langle M \rangle} \frac{dM}{dt} \left( \frac{M(t)}{M_{min}} \right)^{-x} (x-1)\delta t.$$

We transform the integral, by change of variables, from time  $t$  to mass  $M$ ,

$$\int_{M(t_{min})}^{M(t_{max})} dM \frac{SFR}{\langle M \rangle} \left( \frac{M(t)}{M_{min}} \right)^{-x} (x-1)\delta t,$$

and solve the integral, which results in Equation 2.

This paper has been typeset from a  $\text{\TeX}/\text{\LaTeX}$  file prepared by the author.

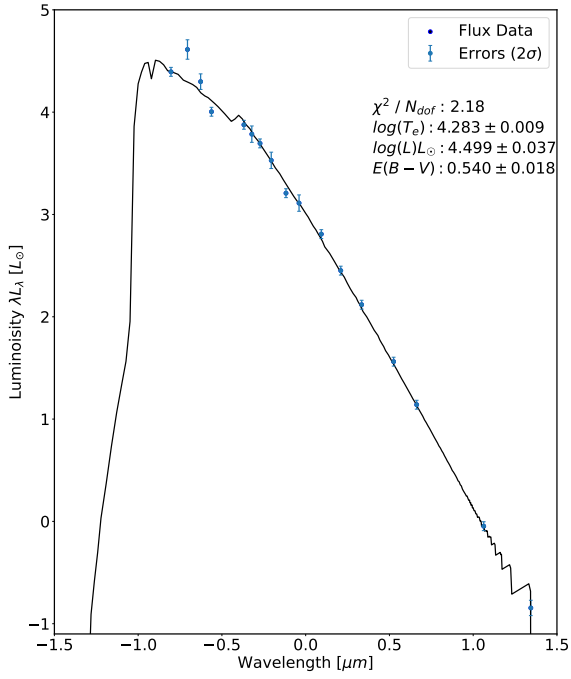


**Figure A3.** The SED of the B1III C star HD 36547.

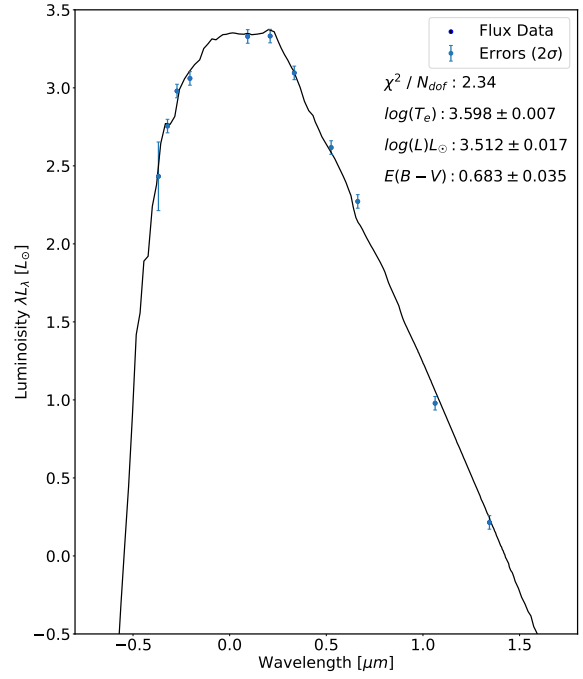


**Figure A4.** The SED of IRAS 5310+2411 which has no spectral classification.

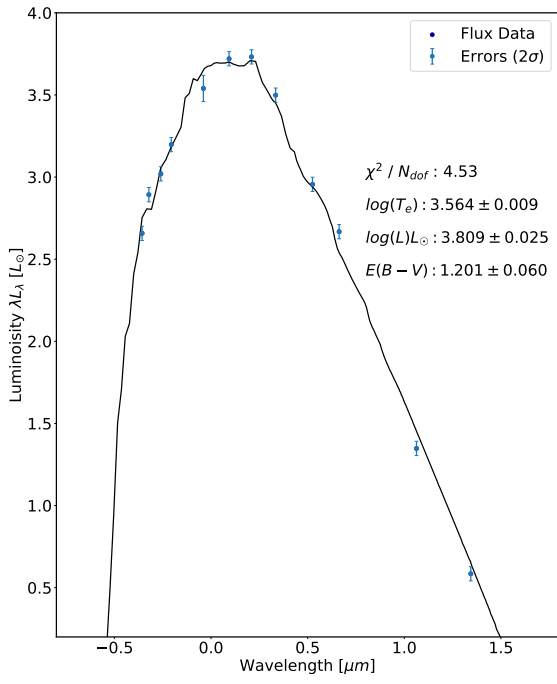


**Figure A5.** The SED of long period variable candidate star IRAS 5361-2406. It has no spectral classification.